ORIGINAL ARTICLE

The Lemnos 8 January 2013 (M_w=5.7) earthquake: fault slip, aftershock properties and static stress transfer modeling in the north Aegean Sea

Athanassios Ganas · Zafeiria Roumelioti ·
Vassilios Karastathis · Konstantinos Chousianitis ·
Alexandra Moshou · Evangelos Mouzakiotis

Abstract We investigate mainshock slip distribution and aftershock activity of the 8 January 2013 M_w=5.7 Lemnos earthquake, north Aegean Sea. We analyse the seismic waveforms to better understand the spatio-temporal characteristics of earthquake rupture within the seismogenic layer of the crust. Peak slip values range from 50 to 64 cm and mean slip values range from 10 to 12 cm. The slip patches of the event extend over an area of dimensions 16×16 km^2. We also relocate aftershock catalog locations to image seismic fault dimensions and test earthquake transfer models. The relocated events allowed us to identify the active faults in this area of the north Aegean Sea by locating two, NE–SW linear patterns of aftershocks. The aftershock distribution of the mainshock event clearly reveals a NE–SW striking fault about 40 km offshore Lemnos Island that extends from 2 km up to a depth of 14 km. After the mainshock most of the seismic activity migrated to the east and to the north of the hypocenter due to (a) rupture directivity towards the NE and (b) Coulomb stress transfer. A stress inversion analysis based on 14 focal mechanisms of aftershocks showed that the maximum horizontal stress is compressional at N84°E. The static stress transfer analysis for all post-1943 major events in the North Aegean shows no evidence for triggering of the 2013 event. We suggest that the 2013 event occurred due to tectonic loading of the North Aegean crust.

**Keywords** Aegean · Stress transfer · Earthquake · Slip model

1 Introduction

On 8 January 2013 at 14:16:08.3 UTC, a moderate earthquake of magnitude M_w=5.7 occurred off the southern coast of Lemnos (Fig. 1; Northern Aegean Sea). The event was strongly felt in nearby north Aegean islands, the neighboring Turkish coasts and the northeastern Greek mainland but caused no damage (Kalogeras et al. 2013). The epicenter was located at 39.67° N, 25.56° E, depth=31 km according to National Observatory of Athens (NOA) online catalogue (M_L= 5.8). The earthquake was well recorded by the Greek seismological networks with a preliminary MT solution (60°/86°/−168°; http://bbnet.gein.noa.gr/HL/seismicity/moment-tensors/), indicating a strike–slip type of seismic motion (Kiratzi and Svigkas 2013). The location of the earthquake indicates that it ruptured a fault segment running south of the North Aegean Trough near the island of Lemnos (Brooks and Ferentinos 1980; Koukouvelas and Aydin 2002; Müller et al. 2013; Fig. 1), where the main, northern branch of the North Anatolian Fault (NAF) enters Aegean Sea (Hatzfeld

A. Ganas (✉) · V. Karastathis · K. Chousianitis ·
A. Moshou · E. Mouzakiotis
Institute of Geodynamics, National Observatory of Athens,
Lofos Nymfon, Thission, 11810 Athens, Greece
e-mail: aganas@noa.gr

Z. Roumelioti
Research Unit of Soil Dynamics and Geotechnical Earthquake
Engineering, Department of Civil Engineering, Aristotle
University of Thessaloniki,
Thessaloniki, Greece

Fig. 1 Geophysical map of the north-central Aegean region showing the location of the 2013 Lemnos earthquake sequence. Beach balls indicate focal mechanisms of post-1943 earthquakes (*M*>5.6) with compressional quadrant in blue (numbering of beach balls is as in Table 3). *Solid triangles* represent HUSN seismic stations used in the slip inversion and *gray dashed lines* indicate graphically the source-station azimuths. Station EDC belongs to KOERI and is discussed in the text
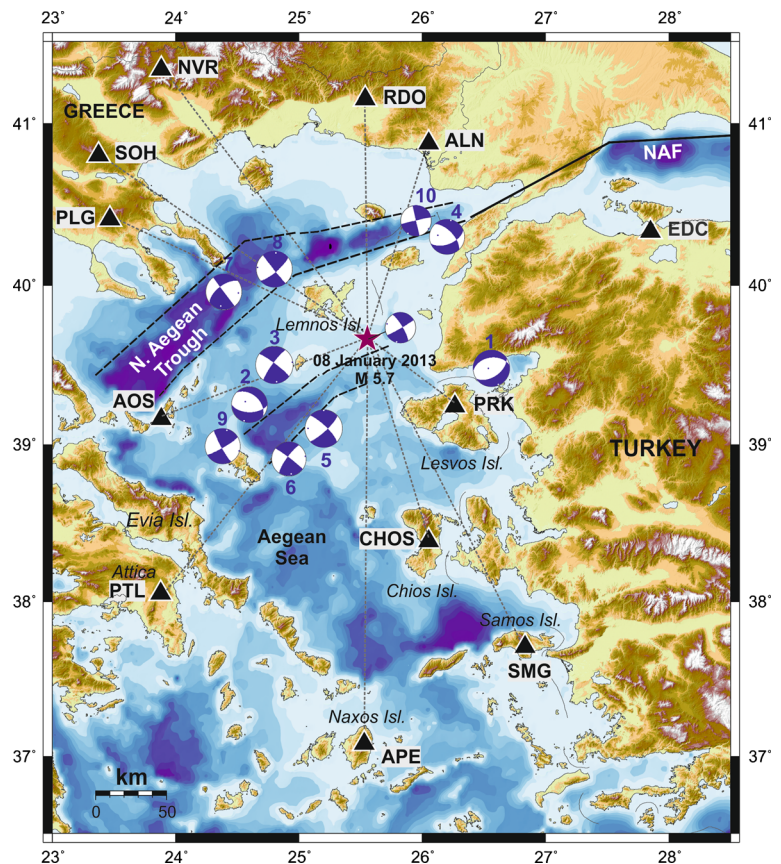
et al. 1999; Karabulut et al. 2006; Caputo et al. 2012). North Aegean is a seismically active area where more than 16 events with *M*>6.5 have occurred since the mid-19th century (Papadopoulos et al. 2002; see references therein). The prominent features are several splays of the NAF that are aligned in a general ENE–WSW orientation with similar kinematics (right-lateral slip; Taymaz et al. 1991; Koukouvelas and Aydin 2002; Yaltirak and Alpar 2002; Kreemer et al. 2004; Müller et al. 2013; Chatzipetros et al. 2013; Fig. 1). Antithetic faulting to the E–W compression is provided by left-lateral shear on NW–SE striking faults (Pavlides and Tranos 1991; Ganas et al. 2005).

This paper presents (a) a relocation analysis of seismological data of the studied sequence collected by NOA (we processed 495 earthquakes during the period 8 January 2013–18 March 2013), (b) a computation of MT solutions for larger aftershocks, (c) a study of the distribution of slip on the ruptured fault during the 8 January 2013 *M*w=5.7 earthquake and (d) results from an earthquake triggering model (based on static stress transfer) for this sequence.

Our main findings include (a) the identification of the NE–SW striking south-dipping plane as the 8 January 2013 slip plane, (b) the mapping of fault slip distribution during this earthquake and c) the imaging of a parallel, NE–SW striking active fault, which was reactivated because of Coulomb stress transfer. These results confirm the right-lateral character of earthquake slip to east of the strong, 1968 Agios Efstratios earthquake (Pavlides and Tranos 1991), which is a low-strain area in the north Aegean Sea (Kreemer et al. 2004).

2 Data analysis

2.1 Relocation of seismic events

The mainshock of 8 January 2013 (*M*w=5.7) and the aftershock sequence of 495 events (1<*M*<4.5; Fig. 2e) of the following 2-month period after the mainshock have been relocated. After a thorough testing of possible velocity models, the 1-D velocity model proposed by

Panagiotopoulos et al. (1985) has been selected for the hypocenter determination of the sequence. The other models tested include the one used by NOA in routine locations, and another one proposed by Karagianni et al. (2005). The phase dataset of NOA used includes more than 5,900 P- and 2,500 S-wave arrivals. The hypocenter location has been based on the algorithm "nonlinloc" of Lomax et al. (2000). This algorithm can support both 1-D and 3-D velocity models. It follows the probabilistic formulation of inversion (Tarantola and Valette 1982; Tarantola 1987). Travel times between each station and all nodes of the location grid are calculated using a 3-D version (Le Meur 1994; Le Meur et al. 1997) of the eikonal finite difference scheme presented by Podvin and Lecomte (1991). A complete probabilistic solution is expressed as a posterior density function (PDF) calculated using the Equal Differential Time (EDT) likelihood function. This function is much more robust in the presence of outliers than the least-square L1 and L2 norms of the misfit between observed and calculated travel times for each observation, usually used by other algorithms. It has also the advantage of being independent of the origin time, thus the 4-D problem of hypocenter location reduces to a 3-D search over spatial location of the hypocenter (latitude, longitude and depth). The complete PDF distribution is obtained using the Oct-Tree importance sampling algorithm that can successively recover multiple PDF minima due to its non linear nature. A detailed description of the "nonlinloc" method can be found in Lomax et al. (2000).

In the present case, we used more than 100 seismographic stations of the Hellenic Unified Seismograph Network (HUSN) for the events relocation. For each phase pick a quality value and a time uncertainty in seconds were assigned. Only events with at least 5 P- and 1 S-wave arrival, having azimuthal gap lower than 180°, location RMS lower than 1.5 s (Fig. 2) and travel time residual (i.e., difference between calculated and observed travel-time) lower than 1.5 s were selected for processing. Given this condition, the final dataset consisted of 495 events located with 1.9 km average value of horizontal location error and 2.3 km vertical. For the selected events station delays were calculated. The selected events were then relocated and the calculated station delays

were added. The processing based on the model of Panagiotopoulos et al. (1985) was the one with the lower average RMS value, smaller confidence ellipsoid volume and a more realistic depth distribution of the hypocenters. In Fig. 2a–d, we show statistical diagrams from the relocated data, i.e., the depth and RMS distribution, while in Fig. 3 we present the relocated seismicity map and cross-sections. To provide a measure of the improvement of the locations after the afore-described analysis, we note that the average RMS (root mean square solution of the 495 relocated events) dropped from 0.45 s before the relocation to 0.29 s afterwards (see also Fig. 2c and d for the distribution of the RMS error values).

The relocated events allowed us (a) to identify two active faults in this area of the north Aegean Sea by locating linear patterns of aftershocks and (b) to analyse post-seismic evolution of seismicity on the 2013 fault planes. The relocated aftershock activity of the 2013 event clearly reveals a NE–SW striking fault about 40 km offshore Lemnos Island (Fig. 3a) that extends from 2 km up to a depth of 14 km (Fig. 3b,c). The aftershock hypocenters are well clustered and indicate the activation of two, parallel faults, striking NE–SW, and located 4 km apart. The existence of two separate faults (Fig. 3a) is supported by the fact that the distance between them is much greater than the average maximum lateral location error (only 1.9 km) and the 67 % confidence ellipsoids do not overlap (Fig. 3d). This image of seismicity highlights the resolving power of the relocation procedure used. However, this consideration is valid only under the assumption that there is not any abrupt lateral anomaly in the local velocity structure. We note that the separation of the parallel fault structures is also visible in case of use of other different 1-D models to locate the events. However, those models do not produce such small lateral location errors and, therefore, cannot support so strongly the existence of the two separate faults.

The orientation of the southern and longer (16 km; Fig. 3a) fault plane matches well the geometry of the NE–SW nodal plane (strike=60°, dip=86°, rake=−168°) in the moment tensor solution of the 8 January 2013 M_w=5.7 event published by NOA (http://bbnet.gein.noa.gr/mt_solution/2013/130108_
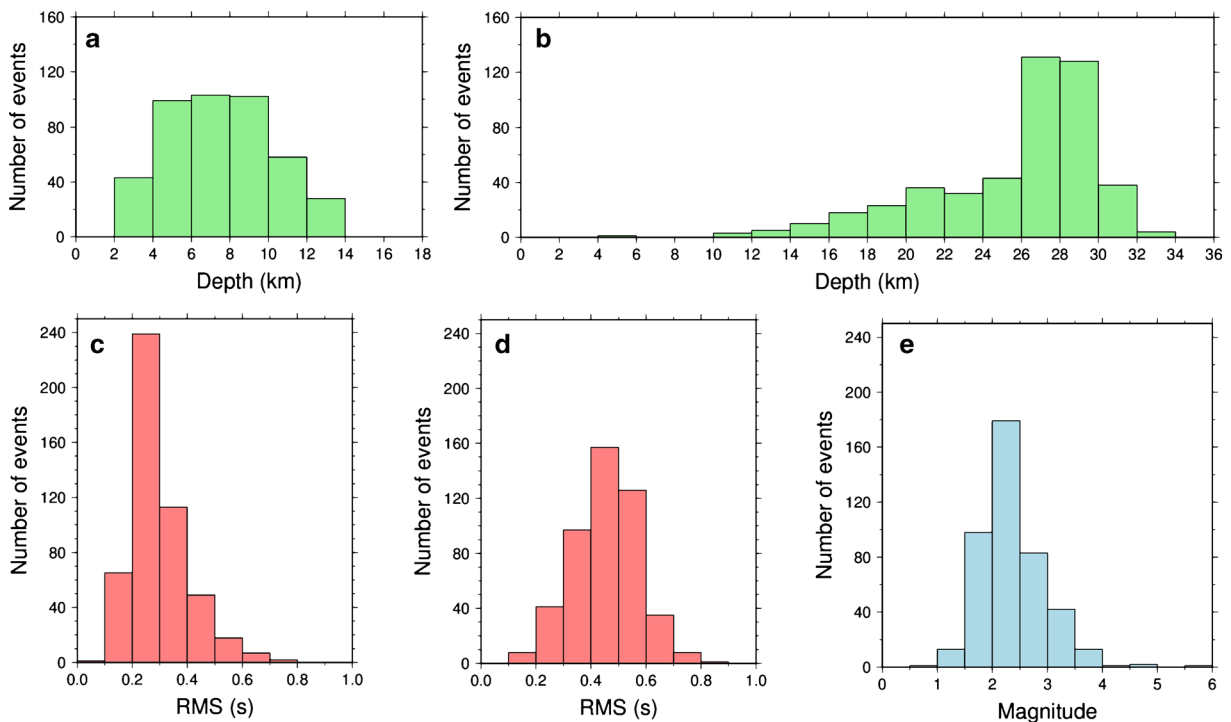
Fig. 2 Diagrams showing descriptive statistics of the aftershock sequence: depth distribution before relocation **a** and **b** after, **c** and **d** RMS error of relocation, **e** histogram of magnitude distribution of events

14_16_08.00_MTsol.html). A total of 88 events spanning a NE–SW distance of 10-km occurred between 8 January and 19 March 2013 on the northern fault, mostly after 20 January 2013 (Fig. 3d,e). Both fault planes delineated in Fig. 3a are optimally oriented to the regional tectonic stress (maximum horizontal stress is compressional in the range N80°E to N120°E; Kreemer et al. 2004; Ganas et al. 2005; Müller et al. 2013; this study).

2.2 MT solutions of strong aftershocks

We applied the Time-Domain Moment Tensor INVersion method (TDMT_INV; Dreger and Helmberger 1993; Pasyanos et al. 1996; Dreger 2002, 2003) to compute the moment tensors of the stronger events of the 8 January 2013 earthquake sequence. As stronger events, we describe those that provided broad-band seismological records at HUSN stations with signal-to-noise ratio greater than 2 at frequencies 0.05–0.08 Hz. This frequency range was used in the band-pass filtering of full waveforms of the three recorded components of motion that were inverted to derive the

moment tensor. In the applied version of the TDMT_INV code, the tensor is decomposed into a scalar seismic moment, double couple (DC) orientation components and a percentage of compensated linear vector dipole (CLVD). Synthetics for the three fundamental faults are combined with an appropriate 1-D velocity model, which in our case is the one proposed by Novotný et al. (2001), to form a library of Green's Functions, computed with the code of Saikia (1994), which are used to match the observed waveforms. The model of Novotný et al. (2001) has been repetitively selected as the most appropriate one for reproducing the entire wave-field at long periods in the broader Aegean area (e.g., Tselentis and Zahradnik 2000; Konstantinou et al. 2010; Roumelioti et al. 2011). In most of the herein presented application of the TDMT_INV we inverted a time window of 120 s, although this could vary (down to 40 s) depending on the magnitude of the event or the signal/noise ratio, i.e., in cases when a second event follows closely in time we are forced to shorten the inverted time window of the studied event. The quality of a solution is determined by the goodness of the fit between synthetic (s) and observed (d) waveforms,
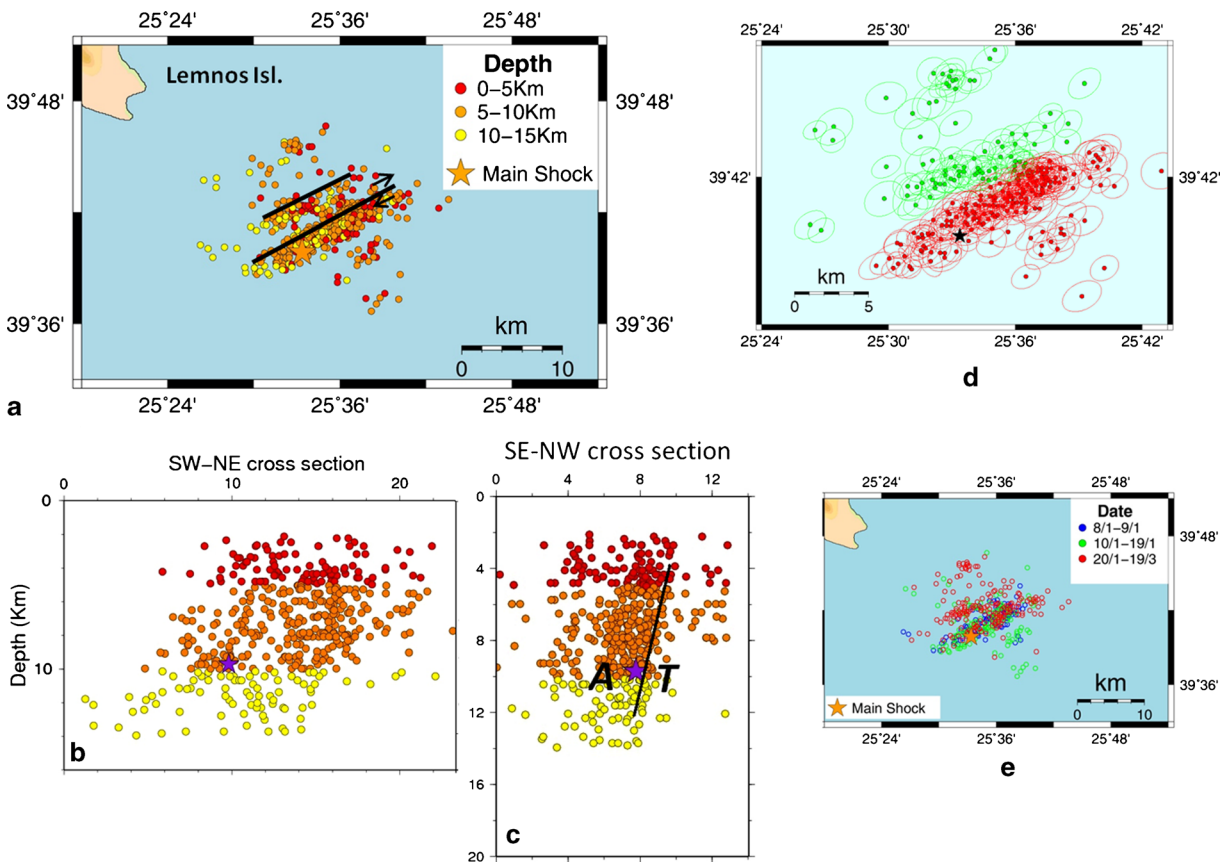
Fig. 3 **a** Seismicity map of the 2013 Lemnos earthquake and vertical cross-sections, parallel (**b**) and normal (**c**) to main fault strike; **d** 67 % confidence error of aftershock locations (*red* indicates main fault; *green* indicates secondary fault) and **e** time distribution of epicenters. *Black lines* indicate the parallel faults that were activated during the sequence. The *black line* in **c** indicates the inferred position of the activated fault plane, together with letters *A* (Away) and *T* (Towards) signifying sense of horizontal motion

which is quantified through the Variance Reduction (VR; Eq. 1), a measure defined as:

$$\mathrm{VR} = \left(1.0 - \frac{\int [d-s]^2 \, \mathrm{d}t}{\int d^2 \, \mathrm{d}t} \right) \times 100 \qquad (1)$$

Regarding the optimum depth for each event, the inversion is run with the point source depth at various levels (incremental step of 1 km within the range 1–20 km). The optimum solution is identified as the one for which both the variance reduction and the percentage of DC are maximized. Solutions obtained by the use of the afore-described method are summarized in Table 1, while corresponding "beach balls" are shown in Fig. 4. The detailed MT solutions of the 14 studied events are included in the Appendix. It should be noted

that we present only high quality solutions, i.e., those that have VR>80 % and at least three stations contributing to them. The results of the applied modeling include 14 focal mechanisms. Most computed tensors are in agreement with the moment tensor of the mainshock (Table 2), implying almost pure dextral strike–slip faulting in the majority of cases. A clear deviation from this general rule appears to be the late aftershock of 5 March (event 14 in Table 1), which shows a stable solution of normal faulting with a strike–slip component.

We then used the ZMAP software (Wiemer 2001) to invert the focal mechanism data for the regional stress tensor applying Michael's Method option (Michael 1991). Results are displayed in a stereographic projection (Wulff net; Fig. 4, inset). The results show low variance (0.06) and a good fit to a homogeneous stress field. The principal stress S1 is horizontal and

Table 1 Source parameters of the 14 studied events

Nr	Origin		Location		M_0 (dyn cm)	M_w	Depth		Plane1			Plane2			VR (%)	CLVD (%)	No. of stations
	Date	Time	Lat (°)	Lon (°)			Catalog	MT	Strike	Dip	Rake	Strike	Dip	Rake			
1	130109	15:36:25.9	39.659	25.510	3.50e+21	3.63	9.1	8	317	78	19	223	72	168	90.2	7	5
2	130109	15:41:32.7	39.687	25.609	5.45e+22	4.46	9.5	8	147	85	−19	239	71	−175	89.3	5	9
3	130109	17:28:11.8	39.696	25.600	2.60e+21	3.54	10.0	9	124	74	−22	220	69	−163	89.1	5	3
4	130110	00:04:46.9	39.703	25.621	1.00e+21	3.28	5.3	3	312	79	−2	43	88	−169	82.6	2	3
5	130110	05:49:58.4	39.657	25.529	6.10e+21	3.79	8.6	3	320	65	9	226	82	155	90.2	0	5
6	130110	10:42:30.7	39.669	25.535	1.60e+21	3.41	10.0	9	323	79	−2	53	88	−69	83.0	1	5
7	130111	00:30:20.6	39.644	25.518	3.00e+22	4.25	11.4	11	331	78	−1	62	89	−168	91.1	6	5
8	130111	15:07:31.7	39.682	25.583	4.80e+21	3.72	11.4	8	299	81	−3	30	87	−171	81.3	8	5
9	130112	13:47:39.3	39.684	25.601	2.40e+21	3.53	10.9	5	297	76	−14	31	77	−166	87.7	9	3
10	130113	08:55:15.0	39.645	25.517	6.60e+22	4.48	13.8	6	334	77	10	241	80	167	87.6	2	8
11	130119	15:19:05.2	39.729	25.442	2.00e+21	3.46	10.7	6	307	80	6	216	84	170	86.9	1	3
12	130119	19:26:41.0	39.692	25.606	3.10e+21	3.60	9.3	5	305	88	1	215	89	178	88.9	5	4
13	130210	18:10:42.5	39.702	25.574	6.40e+21	3.81	13.7	2	312	80	−3	42	87	−170	85.6	5	5
14	130305	09:44:33.8	39.694	25.550	4.90e+21	3.73	13.4	10	321	53	−30	70	67	−139	86.2	2	4

Columns (from left to right) show: event number, date and time of origin, latitude and longitude of the epicenter, seismic moment, moment magnitude, strike dip and rake of the two nodal planes, variance reduction (VR), percentage of CLVD and number of stations used in the MT inversion
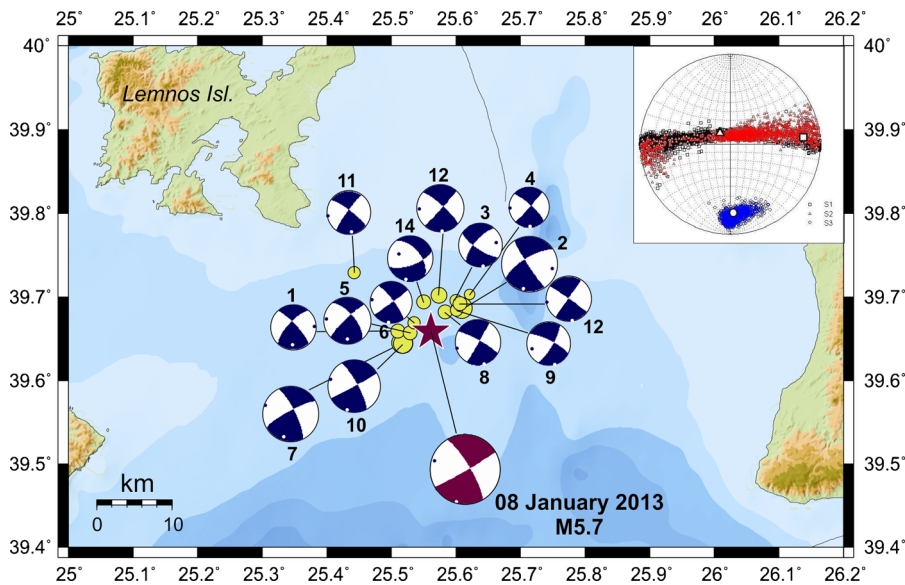
Fig. 4 Focal mechanisms of the largest aftershocks of the 8 January 2013 earthquake sequence, as computed by the TDMT method. Numbers are as in Table 1. The mainshock moment tensor solution is adopted from the online catalog of NOA (http://bbnet.gein.noa. gr). *Inset*: stress inversion results in stereographic projection with Sigma1 (*square*), Sigma2 (*triangle*), Sigma3 (*circle*)

compressional, trending N84°E and plunging 11 degrees. The other two stress axes are (azimuth, plunge) S2: N41°W/70°, S3: N177°E/15°.

2.3 Rupture process and slip distribution

2.3.1 Method

To investigate the slip distribution of the largest event of the sequence, we combined two methods. The empirical Green's functions (EGFs) deconvolution method (Hartzell 1978) was initially applied to compute the Source Time Functions (STFs) of the target event, i.e., the event to be studied in terms of its slip distribution. By deconvolving a smaller, nearby event of similar focal mechanism, we empirically remove path propagation and site effects and obtain the relative, to the deconvolved earthquake, STF of the target event. Then, an inversion method (Mori and Hartzell 1990; modified by Dreger 1994) is applied to back-propagate the computed STF shapes onto the assumed fault plane. During the inversion we put a slip positivity constraint, as well as a smoothing operator which minimizes the spatial derivative of slip. The weight of the smoothing is determined by trial and error by finding the smallest value that provides a smoothed model, as well as maximum fit to the empirically derived STFs. As a result of the inversion procedure we obtain a distribution of slip weights, w_j, that can be interpreted to actual slip values, u_j, through the relation:

$$u_j = \frac{M_0 \cdot w_j}{A \cdot \mu}, \tag{2}$$

where A is the subfault area, μ is the shear modulus, herein taken equal to 3.5×10^{10} Pa, and M_0 is an independently

Table 2 Source parameters of the four events that were used in slip inversions

Abbr.	Date	Origin time	Latitude (°)	Longitude (°)	h (km)	M_L	M_w	10*24	Strike (°)	Dip (°)	Rake (°)
Main	130108	141608.5	39.6642	25.5561	9.7	5.8	5.7	4.392	60	86	−168
Aftershock 1	130110	054958.7	39.6565	25.5292	8.6	3.8	3.8	0.005	54	86	−166
Aftershock 2	130111	003021.1	39.6437	25.5182	11.4	4.4	4.2	0.026	67	62	−173
Aftershock 3	130113	085515.2	39.6452	25.5165	13.8	4.8	4.4	0.057	65	86	−170

Locations were defined in the frame of the present study, while seismic moment (and resulting M_w), strike, dip and rake values are from the online catalog of NOA (http://bbnet.gein.noa.gr)

determined value of the seismic moment of the target event. The uncertainty in the computation of the adopted M_0 value is inherited in the final slip values, e.g., an overestimated M_0 will result in overestimated absolute slip values and vice versa.

The applied methodologies have been thoroughly described in previous publications (e.g., Dreger 1994; Roumelioti et al. 2003). The reader is referred to the aforementioned pertinent literature for more details on the background physics and mathematics.

2.3.2 Data

We compared locations and moment tensors (http://bbnet. gein.noa.gr/HL/seismicity/moment-tensors) of the mainshock and of the largest aftershocks of the sequence to identify those events that are most appropriate to be used as EGFs. An EGF must be co-located to the examined event, of similar focal mechanism and of magnitude large enough to be well recorded at the examined distances but with its time function short compared to the mainshock time function. We identified three events that fulfill the aforementioned criteria and this presented us with the challenge to use them independently and compare results. The time histories of these events were compared to corresponding data of the mainshock at several stations to ensure the resemblance of the waveforms. Basic source parameters of the three events and of the mainshock are listed in Table 2.

For the events of Table 2, we collected three-component broadband velocity time series from the HUSN and the Kandilli Observatory and Earthquake Research Institute (KOERI). Among the wealth of available records, we chose a subset of stations located at distances 30–150 km from the epicenter, which provide satisfactory azimuthal coverage. The distribution of used stations relative to the epicenter of the studied event in presented in Fig. 1. KOERI stations (e.g., EDC in Fig. 1) to the E–NE of the 2013 sequence were carefully examined but could not be included in the inversions due to poor signal-to-noise ratio in their records. So, the largest azimuthal gap in our data set is toward the E–NE and is of the order of 100°. We tried to use the same stations sets for all three target-EGF pairs, although this was not possible in few cases due to noisy or unavailable data (i.e., PRK and APE

stations were not used in the inversions based on Aftershock 2 of Table 2 and PTL station was not used in the inversions based on Aftershock 3 of Table 2).

Original velocity time series were corrected for possible zero-offsets of their mean through a first-order baseline operator and linear trends were removed using the least-squares method. Then, velocity waveforms were integrated to displacement and band-pass filtered in the frequency range 0.01–1 Hz, by using a fourth-order Butterworth filter.

2.3.3 Application and results

Source process of the M_w= 5.7 mainshock Even considering wave scattering, the fault-normal component of ground motion is expected to include the highest amplitudes of SH waves from a near-vertical strike–slip rupture as the one examined in this study. Therefore, we rotated originally east–west and north–south oriented horizontal components to fault-parallel and fault-normal directions and used the fault-normal components to compute the STFs of the studied mainshock. Displacement waveforms of each one of the three EGFs presented in Table 2 were deconvolved from the corresponding waveforms of the mainshock to compute the STFs at the locations of the stations of Fig. 1. In Fig. 5, we present an example of the computed STFs at the three components (fault-normal, fault-
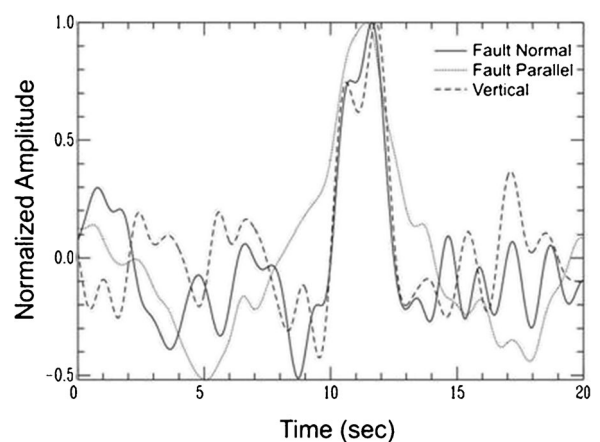

Fig. 5 Comparison of STFs computed using the three different components of motion recorded at station CHOS. EGF in this example is "Aftershock 1" in Table 2

parallel and vertical) of motion at station CHOS. As in the example shown in Fig. 5, in most cases STFs derived from the fault-normal components correlate well with corresponding STFs derived from the vertical components, while the fault-parallel component appears noisier.

In Fig. 6, we compare the STFs computed independently from the three EGF-target pairs. The differences in shapes of the STFs at each station are indicative of the uncertainties introduced in the subsequent step of our analysis, i.e., the inversion for the computation of the slip distribution of the target event. STFs at individual stations compare well to each other despite the fact that the three EGFs are of quite different magnitude. Their duration ranges from approximately 2 s to more than 4 s and in general, STFs to the NE are shorter. This is indicative of some directivity of the earthquake energy toward this direction, although the phenomenon is not strong. At some stations (e.g.,

AOS, CHOS) STFs present two lobes, indicating two distinct slip episodes on the ruptured plane. The STFs computed from the afore-described procedure were normalized to unit area and their shapes were inverted to derive the distribution of slip on the fault plane. The fault plane was modeled as a rectangular area of (20×20) km^2 with 20×20 subfaults along strike and along dip, correspondingly. Considering that the highest inverted frequency is 1 Hz and the adopted crustal shear-wave velocity is 3.4 km/s, the shortest resolvable wavelength is 0.85 km, i.e., smaller than the subfault dimension.

The slip distribution patterns as determined by the use of the three different EGFs are presented in Fig. 7a–c. Absolute slip values were computed from slip weights using Eq. 2 and the mainshock seismic moment value included in Table 2. The similarity of the three patterns is impressive both in terms of the extent of the rupture, as well as the
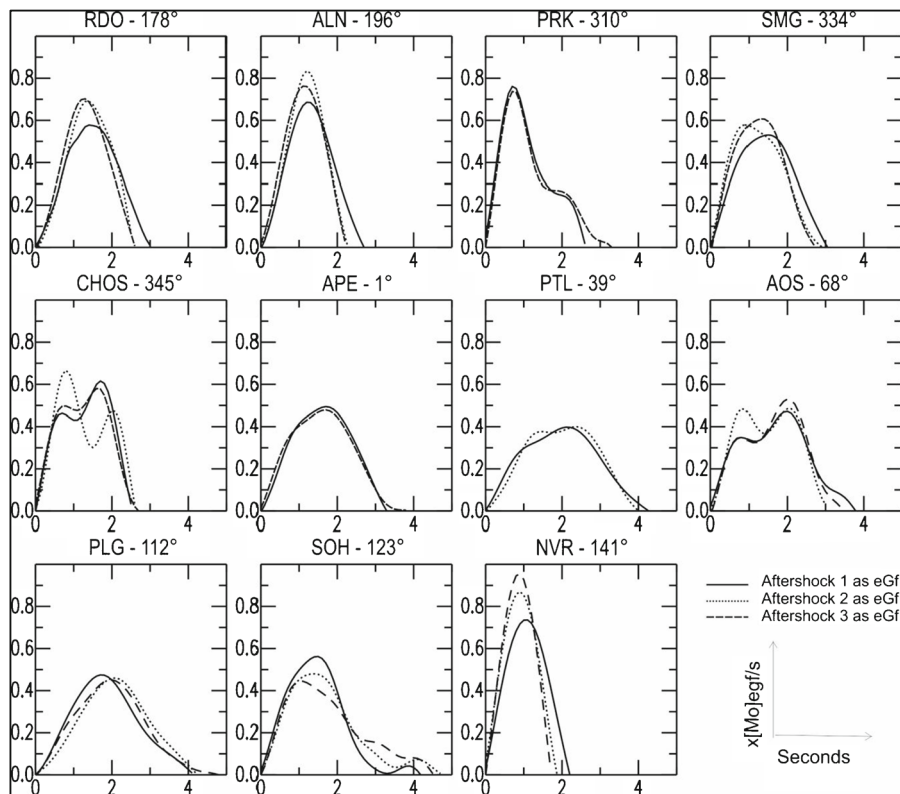
Fig. 6 STFs of the mainshock at the examined stations as computed using three different EGFs (Table 2). All STFs are normalized to unit area. Back azimuth is noted next to each station name
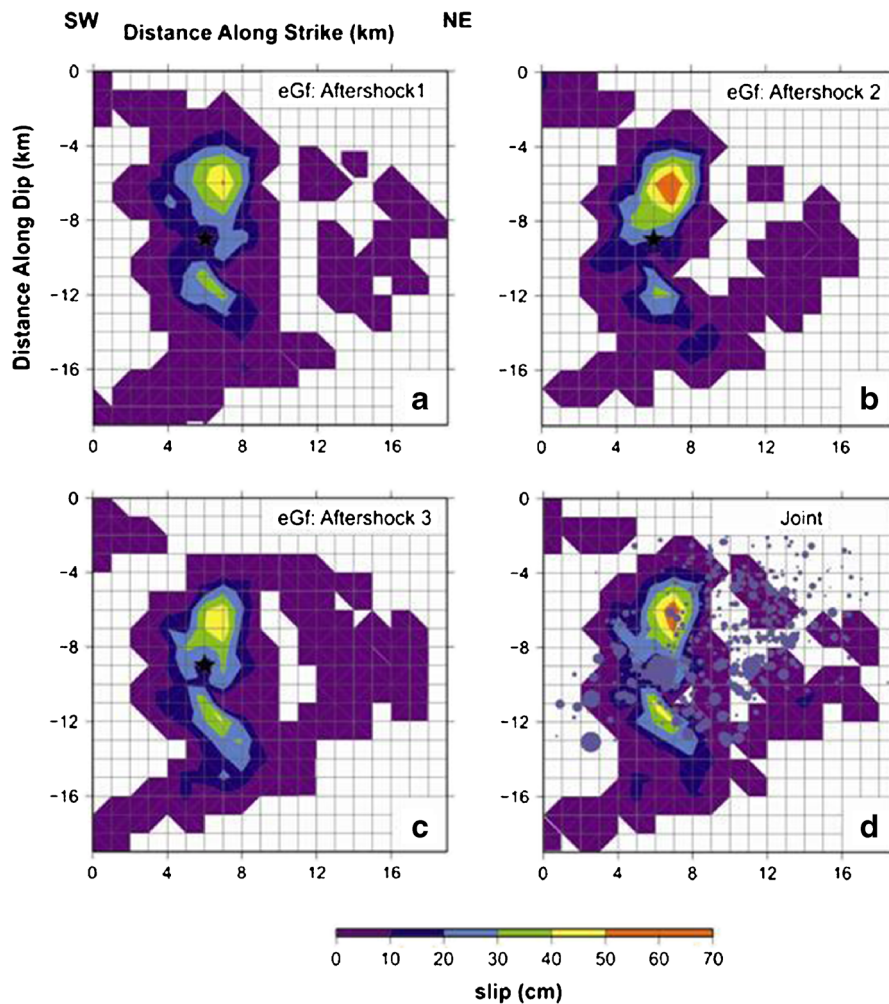
Fig. 7 Static slip distribution pattern on the fault plane of the M5.7 N. Aegean earthquake as derived from the use of three different EGFs: **a** Aftershock 1, **b** Aftershock 2, **c** Aftershock 3 of Table 2. In subplot **d**, the synthetic result from the joint use of the three EGFs is presented with earthquake foci (*circles*) superimposed on the assumed ruptured plane

details of it. In accordance with STFs shapes, two prevailing slip episodes appear to have occurred above and below the assumed earthquake focus (star symbol in Fig. 7), with the shallower concentration being systematically the largest. Peak slip values range from 50 to 64 cm and mean slip values (for the ruptured parts of the assumed fault plane) range from 10 to 12 cm. An interesting feature of these distributions is the eastward extend of the rupture with very low slip values. If results were based on a single EGF, this low-slip area would be questionable. However, in our study its existence is verified by three independent computations. In Fig. 7d, we present the slip

distribution as derived from the joint inversion of all three EGFs. In this plot, we have superimposed on the slip picture the relocated foci of the sequence (open circles, circle diameter relative to the earthquake magnitude). Most aftershocks are concentrated in the aforementioned low-slip area, which is an additional indication that the rupture of the examined event continued to the east of the well-defined slip patches. The slip of the studied event appears to have covered an area of 16×16 km^2. However, in terms of seismic hazard, i.e., strong ground motion generation, what is important is the large concentrations of slip, which in this case are extended more along the width than

along the length of the fault. In Fig. 8, we compare the STFs as have been computed from observed data of Aftershock 2 (Table 2) with those computed synthetically when using the slip distribution model of Fig. 7b.

By comparing the results derived for the mainshock of the 2013 NE Aegean sequence using three different EGFs, we conclude that the accuracy of the applied method is to a large degree insensitive on the choice of the EGF. Of course, EGFs must have been initially chosen based on the similarity of their location and focal mechanism to the ones of the mainshock. The magnitude of the EGF can be quite smaller compared to the magnitude of the examined event, as long as noise-to-signal ratio is sufficient to ensure acceptable levels of noise in the resulting STF.

2.4 Static stress transfer modeling

We model static stress transfer for the January 2013 Lemnos earthquake assuming that failure of the crust occurs by shear, so that the mechanics of the process can be approximated by the Okada (1992) expressions for the displacement and strain fields due to a finite rectangular source in an elastic, homogeneous and isotropic half-space. We use the Coulomb 3.3 software (Lin and Stein 2004; Toda et al. 2005) to compute the static Coulomb stress change (ΔCFF) by assuming a Young modulus of 8×10^5 bar, Poisson's ratio 0.25 and effective coefficient of friction, $\mu' = 0.4$ which is closer to friction values for major crustal faults (Harris and Simpson 1998). The derived slip model of the 8 January 2013 event (Fig. 7d) is then incorporated into the computation of ΔCFF to investigate the loaded and relaxed volumes of the neighbouring crust (Fig. 9). The calculation was done at seismogenic depths (2–14 km range) including the depth of the 8 January 2013 event hypocenter (10 km; Table 2). We have checked the robustness of our results by using μ' values from 0.1 to 0.8. In all cases the spatial distribution of
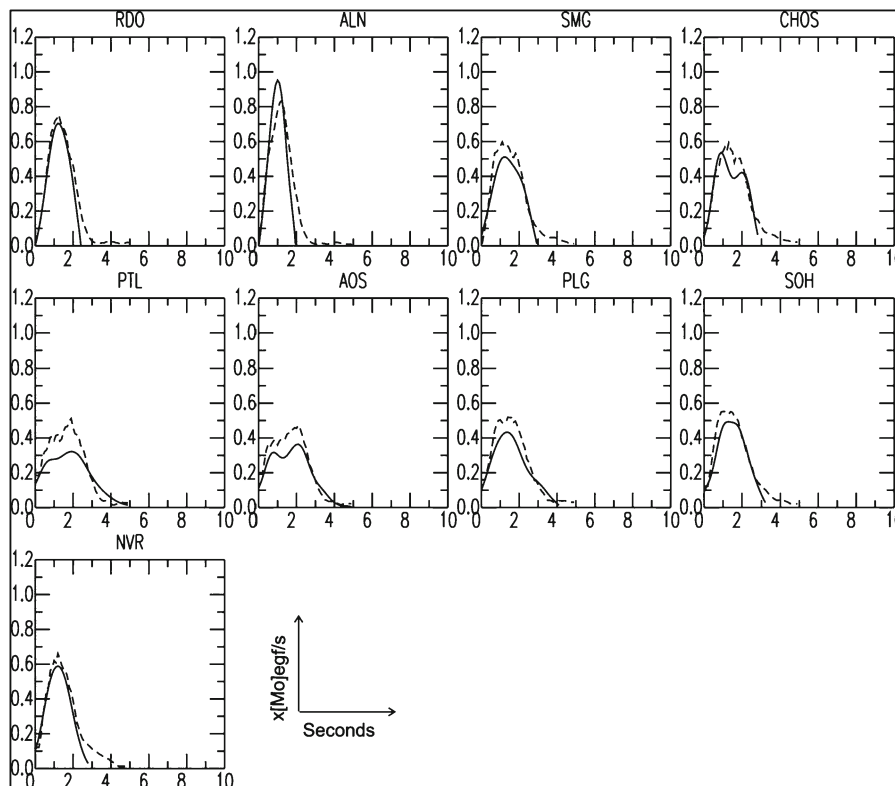
Fig. 8 Comparison of STF shapes (normalized to unit area) computed from data of Aftershock 2 (Table 2) (*continuous lines*) and synthetically, when using the slip distribution model of Fig. 7b (*dashed lines*)
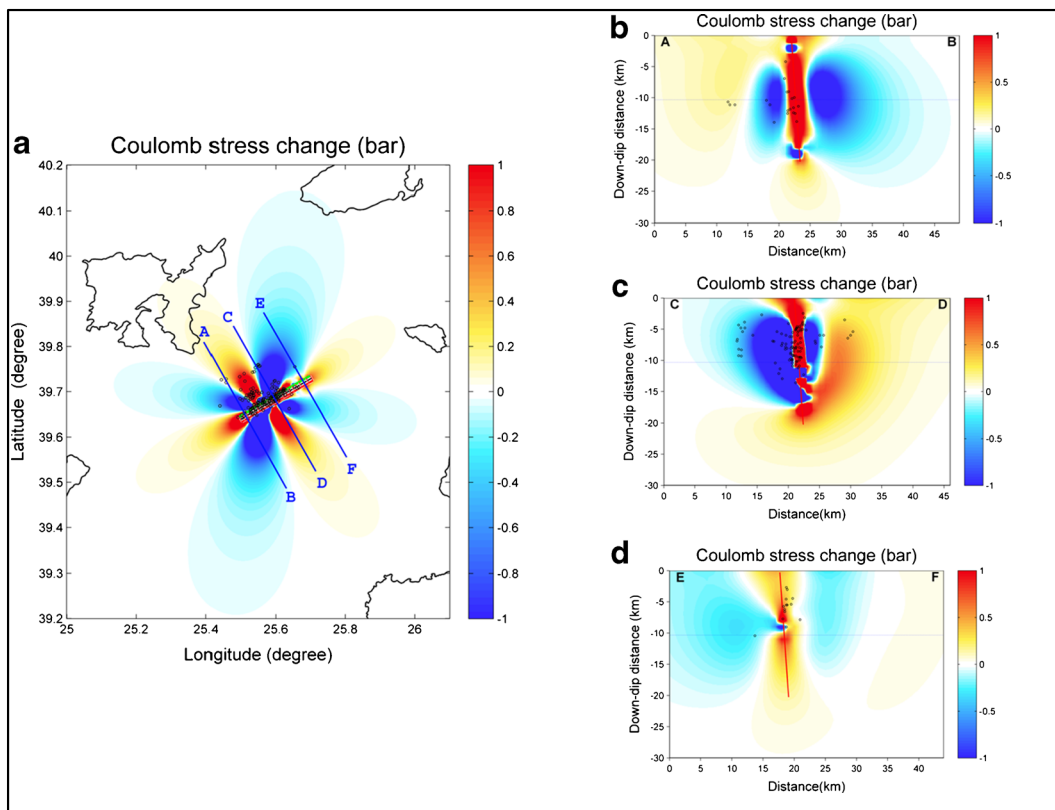
Fig. 9 Coulomb stress changes at 10-km depth associated with the 8 January 2013 (14:16 UTC) M_w=5.7 earthquake (slip model of Fig. 7d). Palette of stress values is linear in the range −1 to +1 bar. *Blue areas* indicate unloading and, *red areas* indicate loading. Colour scale in bar (1 bar=100 kPa). *Open circles* are aftershocks. **a** Map; **b**, **c** and **d** vertical cross-sections normal to fault strike of mainshock (view from the SW)

ΔCFF values does not change significantly compared to the results obtained for μ'=0.4. We interpret a positive value of ΔCFF to indicate that a fault plane occurring within this stress lobe has been brought closer to failure; when ΔCFF is negative, the fault is brought further from failure (i.e., relaxed). In Fig. 9, we show the Coulomb stress distribution at 10 km depth computed on target faults with similar focal mechanisms to the mainshock (option: stress on planes). We observe a relatively good correlation between aftershock locations and positive stress lobes, especially in the volume of crust within 2 km from the modeled fault plane (see orthogonal cross-sections AB, CD and EF). A positive Coulomb stress lobe (ΔCFF >1 bar) is obtained in the area to the north of the 8 January 2013 hypocenter where a parallel fault (shown in Fig. 3a) exists at a mean distance of about 4 km along strike. Some aftershocks also occur inside the relaxed areas (mostly to the north

of the seismic fault depicted in Fig. 9a; mostly left from the fault plane depicted in Fig. 9b,c,d) that are not explained by our stress model but could be due to (a) missed, heterogeneous slip that modifies the static stress transfer change across the fault, (b) on damage in the vicinity of the rupture (brittle microcracking), or (c) dynamic stress triggering (e.g., Gomberg et al. 2001).

Furthermore, we investigated if the 2013 earthquake occurred in a region brought closer to failure by previous, post-1943 earthquakes in the north Aegean (see Table 3 for events of M_w>5.6 and known focal mechanisms). The earthquakes before 1944 were not considered due to the larger uncertainty in their focal parameters (strike/dip/ rake). This part of the north Aegean region (east–southeast of Lemnos) is empty of large earthquake events (Papadopoulos et al. 2002) and it is close to the boundary between loaded and relaxed crustal areas according to previous models

Table 3 Source parameters of post-1943 strong and shallow earthquakes in the north and central Aegean Sea

No.	Date (YYYYMMDD)	LAT	LON	Depth	M_w	Type	RL (km)	RW (km)	Strike	Dip	Rake	Source
1	19441006	39.48	26.56	10	6.8	N	40	17	56	51	−106	1, 7
2	19670304	39.25	24.60	10	6.6	N	25	13	313	43	−56	2, 3
3	19680219	39.50	24.80	10	6.9	SS	53	16	216	81	173	4
4	19750327	40.45	26.12	15	6.5	SS	29	11	68	55	−145	2, 3
5	19811219	39.10	25.20	10	6.9	SS	53	16	47	77	−167	4, 3
6	19811227	38.91	24.92	6	6.3	SS	21	9	216	79	175	2, 4
7	19820118	39.96	24.39	7	6.6	SS	33	12	233	62	180	2, 3
8	19830806	40.10	24.80	9	6.7	SS	39	13	50	76	177	4, 3
9	20010726	38.99	24.38	12	6.5	SS	32	10	151	83	7	5
10	20030706	40.427	26.103	18	5.7	SS	8	5.5	257	89	−179	6

It is assumed that the fault center is located at hypocenter. Last column indicates source of information as follows: 1, Nalbant et al. (1998); 2, Taymaz et al. (1991); 3, Makropoulos et al. (2012); 4, Kiratzi et al. (1991); 5, Benetatos et al. (2002); 6, Karabulut et al. (2006); 7, Altinok et al. (2012)

(Papadimitriou and Sykes 2001). We calculated cumulative Coulomb stress changes on both (a) optimally oriented planes to regional compression (nearly east–west compression: N84°E, this study) and (b) on planes of fixed orientation assuming that NE–SW striking, right-lateral faults of the 8 January 2013 type-of-rupture will be candidates for failure (see Ganas et al. 2012 for modeling details). The relative results are shown in Fig. 10a and b, respectively. In both cases, we find that no triggering is promoted as the ΔCFF values in the hypocentral

area of the 2013 earthquake are negative (between 0 and −0.5 bar).

We note that the 2013 rupture source area is located near the 19 February 1968 earthquake ($M =$ 6.9; about 60 km to the east; Fig. 1). In this respect, the location of the 1968 earthquake plays a critical role in the sign and amount of the cumulative stress change in the 2013 source area. We considered three possible locations of the 1968 epicenter and we included them in our static stress transfer analysis (Fig. 10). The locations have been
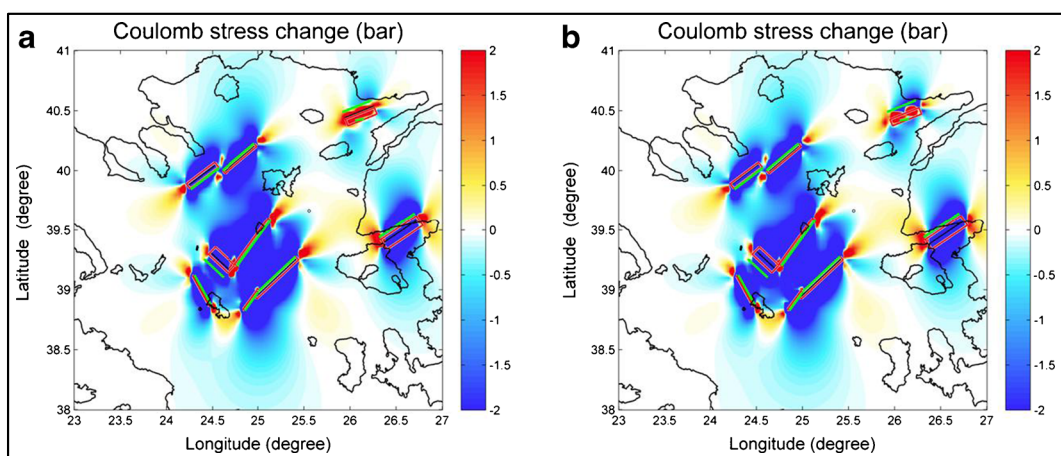
Fig. 10 Coulomb stress changes on 2013-type planes at **a** 8 km and **b** 10-km depth associated with the pre-2013 shallow Aegean earthquakes. Palette of stress values is linear in the range −2 to +2 bar. *Green lines* show the modeled sources (Table 3) and *red*

rectangles are surface projections of fault planes. *Blue areas* indicate unloading, *red areas* indicate loading. Colour scale in bar (1 bar=100 kPa). *Open circle* denotes the location of the 2013 epicenter

considered in the vicinity of the island of Agios Efstratios (Fig. 1), because the field observations published by Pavlides and Tranos (1991) indicate proximity to and/or emergence of the sub-marine seismic fault on the island. In all cases, we found that the 2013 source area remains inside the relaxed area of the cumulative pre-2013 stress change. Another implication is that the 2013 earthquake is located on a different fault, sub-parallel to the 1968 fault shown in the map of Caputo et al. (2012), with similar kinematics (right-lateral slip).

3 Discussion and conclusions

(a) We performed a detailed analysis of the 8 January 2013 earthquake of $M_w=5.7$ and its aftershock sequence, which involved the relocation of 495 events of the sequence ($1<M<4.5$), computation of the moment tensors of the 14 largest magnitude aftershocks, the study of the spatio-temporal distribution of slip during the mainshock and static stress transfer computations. Most of the aftershocks moment tensors indicate rupture characteristics similar to the ones inferred from mainshock moment tensor, i.e., pure or predominant dextral strike–slip faulting (Table 1 and Fig. 4).

(b) Relocated seismicity provided an enhanced picture of the tectonic structures that were involved in the January 2013 North Aegean earthquake sequence, delineating two parallel concentrations of epicenters and thus implying the activation of two parallel faults (Fig. 3a). The southerner fault gathers the majority of aftershock foci, as well as the focus of the mainshock. After the occurrence of the 8 January 2013 $M_w=5.7$ main event, seismic activity migrated to the east and to the north of the mainshock epicenter (Fig. 3e). Accumulation of epicenters on the northerner parallel structure (Fig. 3a,d,e) initiated 1 h 38 min and 39 s after the mainshock (at 15:54:47 UTC of 8 January 2013, $M=2.3$, depth=7.8 km) and this implies that seismic activity on this structure was triggered by the neighboring $M_w=5.7$ event.

(c) The EGF and STF inversion methods were combined to study the slip distribution and inferred rupture process of the $M_w=5.7$ earthquake. The excellent dataset of broadband records of this sequence presented us with a unique opportunity to perform repetitive inversions for the mainshock source process using three different aftershocks as EGF. We resulted in three independent slip distribution patterns and a combined one, which presented impressive similarity to each other, indicative of the stability of our computations. Peak slip values range from 50 to 64 cm and mean slip values (for the ruptured parts of the assumed fault plane) range from 10 to 12 cm. The slip patches of the event extend over an area of dimensions 16×16 km^2. Most of the mainshock slip is elongated along the dip of the fault and to the east of the mainshock. However, low-slip values were consistently derived to the east of the main slip patches, where most of the aftershocks were relocated.

(d) The static stress transfer analysis for all major events in the North Aegean, during the post-1943 period, shows no evidence for triggering of the January 2013 event, either when modeling the static stress on the 2013 fault plane or on optimal planes to regional compression. We suggest that the 2013 event occurred due to tectonic loading of the North Aegean crust.

Appendix

The moment tensor solutions for the 14 events in Table 1, as computed using a time-domain moment tensor inversion method, are shown in detail. For each solution, we present the comparison between observed and synthetic waveforms (continuous and dashed lines, respectively) at the inverted stations. For each station, comparisons are shown for the radial, tangential and vertical components. To the left of each plot, we present a summary of the solution
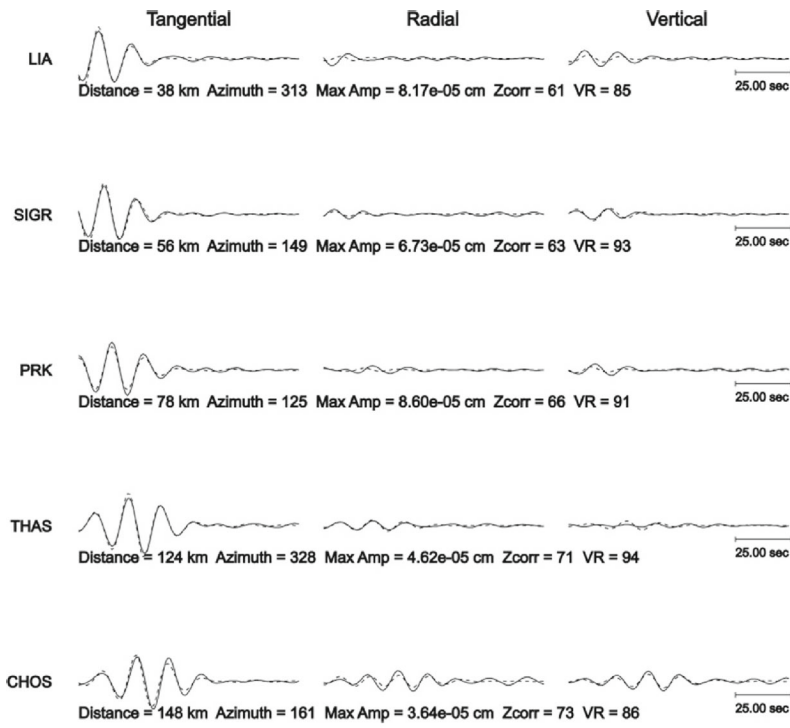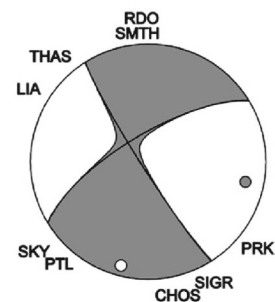
Depth = 8
Strike = 317 ; 223
Rake = 19 ; 168
Dip = 78 ; 72
Mo = 3.50e+21
Mw = 3.63
Percent DC = 93
Percent CLVD = 7
Percent ISO = 0
Variance = 1.87e-11
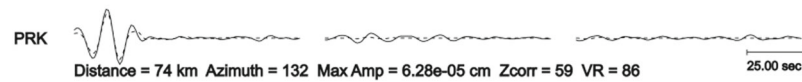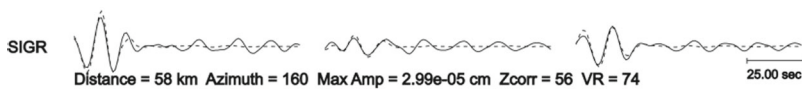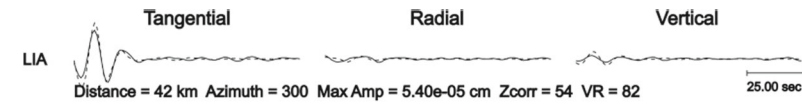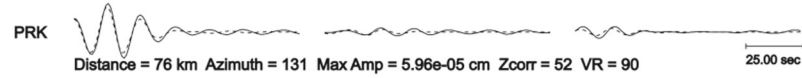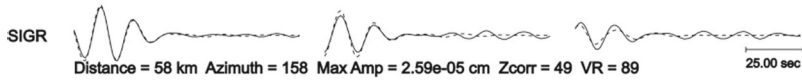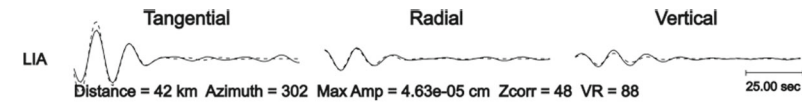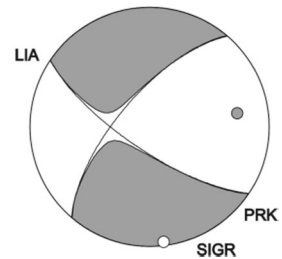Var. Red. = 90.2
RES/Pdc = 2.01e-13
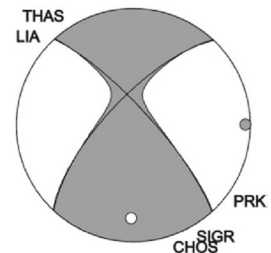
1
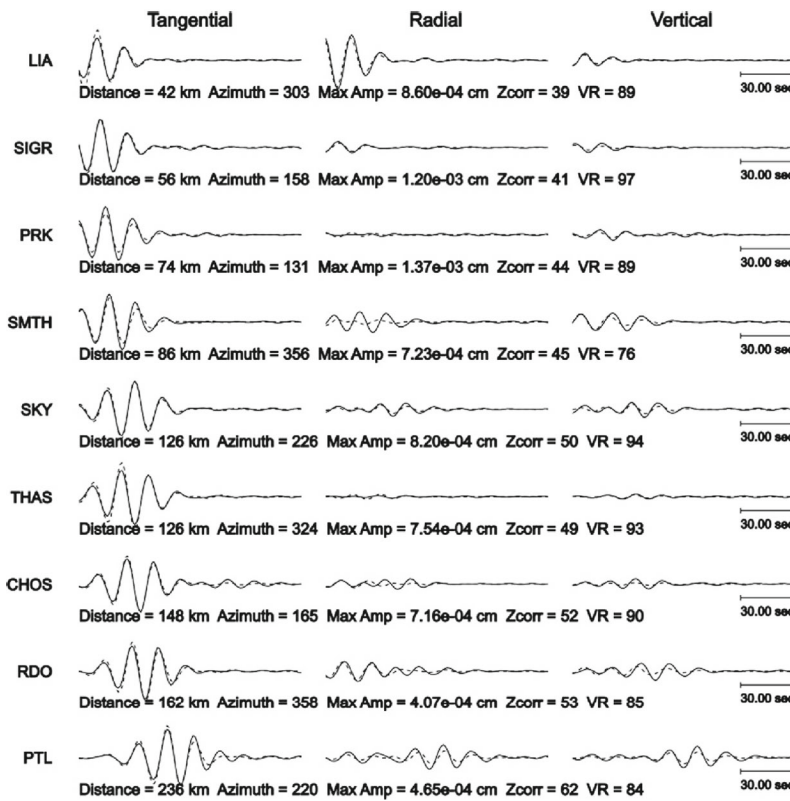
Depth = 8
Strike = 147 ; 239
Rake = -19 ; -175
Dip = 85 ; 71
Mo = 5.40e+22
Mw = 4.43
Percent DC = 95
Percent CLVD = 5
Percent ISO = 0
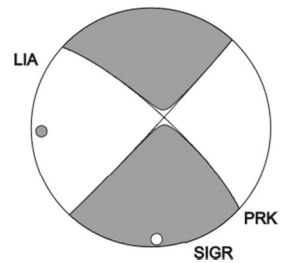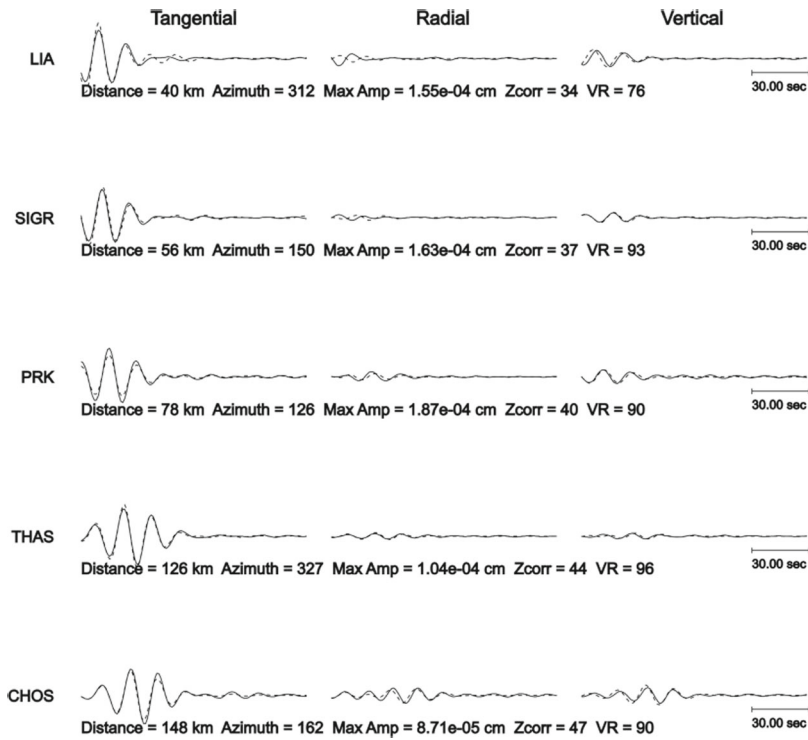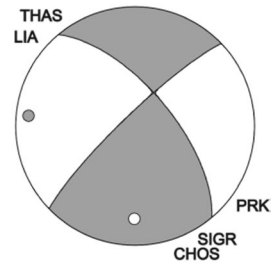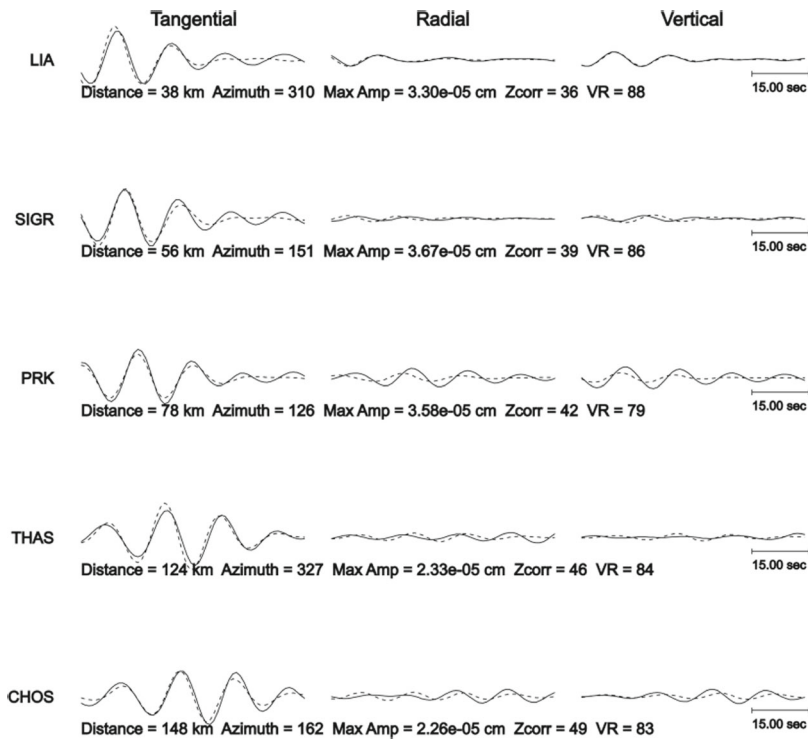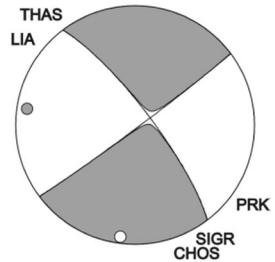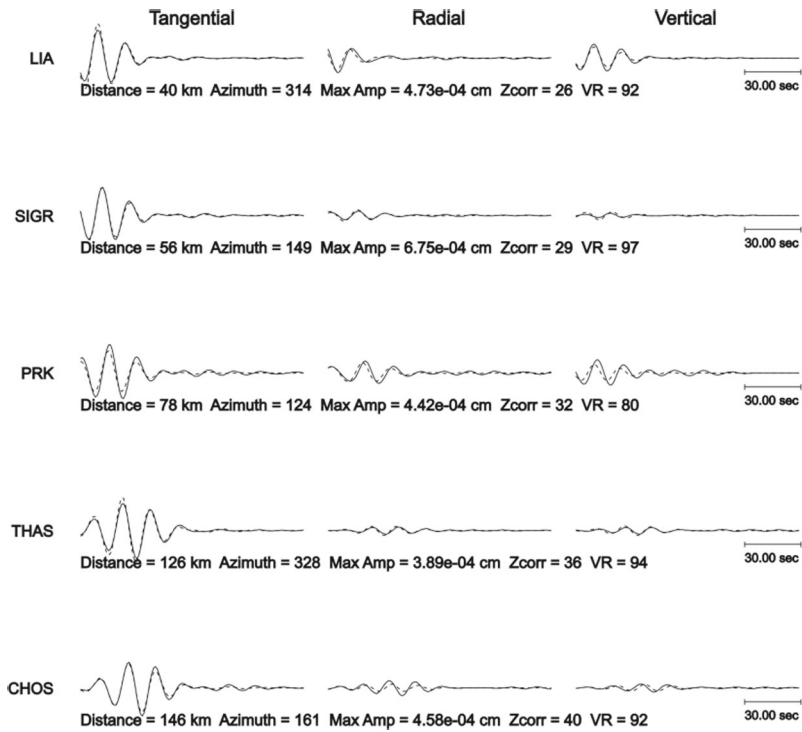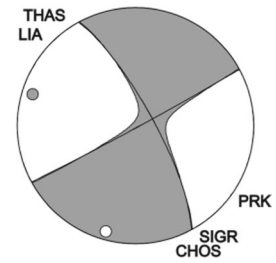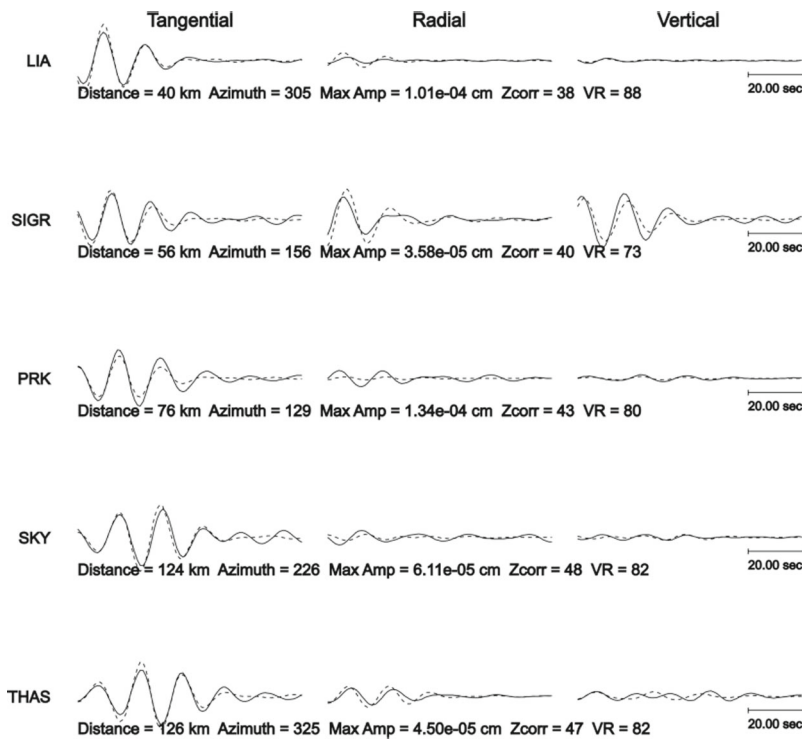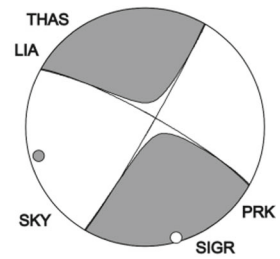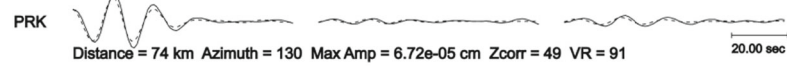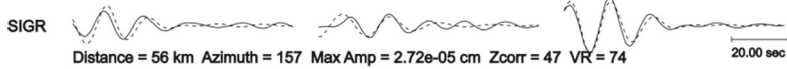Variance = 2.80e-09
Var. Red. = 89.3
RES/Pdc = 2.94e-11

2

LIA

Tangential   Radial   Vertical

Distance = 42 km Azimuth = 302 Max Amp = 4.63e-05 cm Zcorr = 48 VR = 88   25.00 sec

SIGR

Distance = 58 km Azimuth = 158 Max Amp = 2.59e-05 cm Zcorr = 49 VR = 89   25.00 sec

PRK

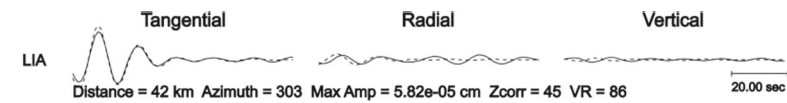Distance = 76 km Azimuth = 131 Max Amp = 5.96e-05 cm Zcorr = 52 VR = 90   25.00 sec
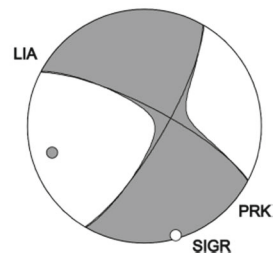
Depth = 9
Strike = 124 ; 220
Rake = -22 ; -163
Dip = 74 ; 69
Mo = 2.60e+21
Mw = 3.54
Percent DC = 95
Percent CLVD = 5
Percent ISO = 0
Variance = 1.05e-11
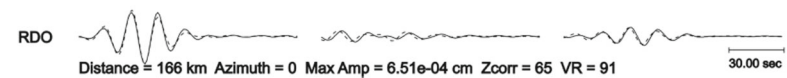Var. Red. = 89.1
RES/Pdc = 1.11e-13

3

LIA

Tangential   Radial   Vertical

Distance = 42 km Azimuth = 300 Max Amp = 5.40e-05 cm Zcorr = 54 VR = 82   25.00 sec

SIGR

Distance = 58 km Azimuth = 160 Max Amp = 2.99e-05 cm Zcorr = 56 VR = 74   25.00 sec

PRK

Distance = 74 km Azimuth = 132 Max Amp = 6.28e-05 cm Zcorr = 59 VR = 86   25.00 sec

Depth = 3
Strike = 43 ; 312
Rake = -169 ; -2
Dip = 88 ; 79
Mo = 1.00e+21
Mw = 3.28
Percent DC = 98
Percent CLVD = 2
Percent ISO = 0
Variance = 1.42e-11
Var. Red. = 82.6
RES/Pdc = 1.45e-13

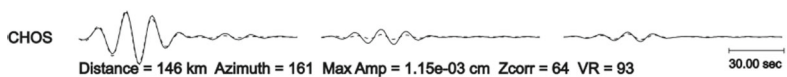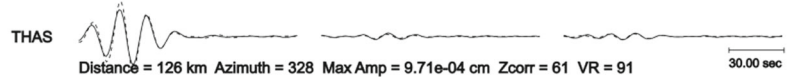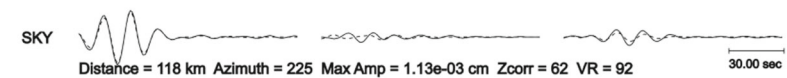**4**

Tangential   Radial   Vertical

LIA
Distance = 40 km Azimuth = 312 Max Amp = 1.55e-04 cm Zcorr = 34 VR = 76   30.00 sec
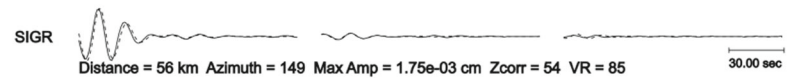
SIGR
Distance = 56 km Azimuth = 150 Max Amp = 1.63e-04 cm Zcorr = 37 VR = 93   30.00 sec

PRK
Distance = 78 km Azimuth = 126 Max Amp = 1.87e-04 cm Zcorr = 40 VR = 90   30.00 sec

THAS
Distance = 126 km Azimuth = 327 Max Amp = 1.04e-04 cm Zcorr = 44 VR = 96   30.00 sec

CHOS
Distance = 148 km Azimuth = 162 Max Amp = 8.71e-05 cm Zcorr = 47 VR = 90   30.00 sec

Depth = 3
Strike = 226 ; 320
Rake = 155 ; 9
Dip = 82 ; 65
Mo = 6.10e+21
Mw = 3.79
Percent DC = 100
Percent CLVD = 0
Percent ISO = 0
Variance = 7.96e-11
Var. Red. = 90.2
RES/Pdc = 7.96e-13

5

Tangential   Radial   Vertical

LIA
Distance = 38 km Azimuth = 310 Max Amp = 3.30e-05 cm Zcorr = 36 VR = 88   15.00 sec

SIGR
Distance = 56 km Azimuth = 151 Max Amp = 3.67e-05 cm Zcorr = 39 VR = 86   15.00 sec

PRK
Distance = 78 km Azimuth = 126 Max Amp = 3.58e-05 cm Zcorr = 42 VR = 79   15.00 sec

THAS
Distance = 124 km Azimuth = 327 Max Amp = 2.33e-05 cm Zcorr = 46 VR = 84   15.00 sec

CHOS
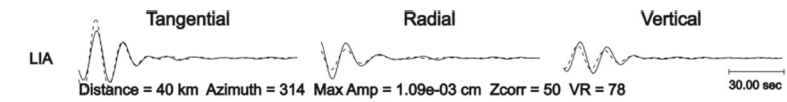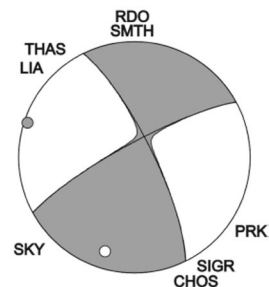Distance = 148 km Azimuth = 162 Max Amp = 2.26e-05 cm Zcorr = 49 VR = 83   15.00 sec

Depth = 9
Strike = 53 ; 323
Rake = -169 ; -2
Dip = 88 ; 79
Mo = 1.60e+21
Mw = 3.41
Percent DC = 99
Percent CLVD = 1
Percent ISO = 0
Variance = 1.20e-11
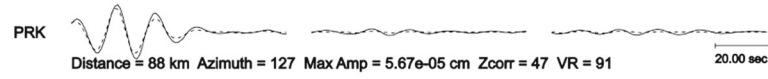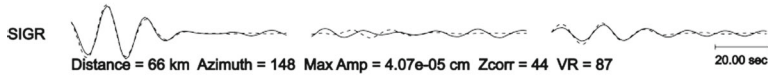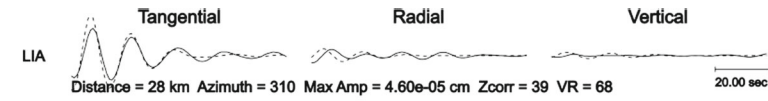Var. Red. = 83.0
RES/Pdc = 1.21e-13

6

Tangential   **Radial**   **Vertical**

LIA
Distance = 40 km Azimuth = 314 Max Amp = 4.73e-04 cm Zcorr = 26 VR = 92   30.00 sec

SIGR
Distance = 56 km Azimuth = 149 Max Amp = 6.75e-04 cm Zcorr = 29 VR = 97   30.00 sec

PRK
Distance = 78 km Azimuth = 124 Max Amp = 4.42e-04 cm Zcorr = 32 VR = 80   30.00 sec

THAS
Distance = 126 km Azimuth = 328 Max Amp = 3.89e-04 cm Zcorr = 36 VR = 94   30.00 sec

CHOS
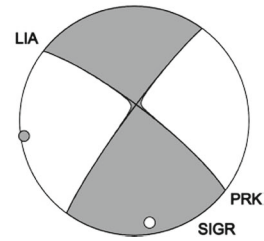Distance = 146 km Azimuth = 161 Max Amp = 4.58e-04 cm Zcorr = 40 VR = 92   30.00 sec

Depth = 11
Strike = 62 ; 331
Rake = -168 ; -1
Dip = 89 ; 78
Mo = 3.00e+22
Mw = 4.25
Percent DC = 94
Percent CLVD = 6
Percent ISO = 0
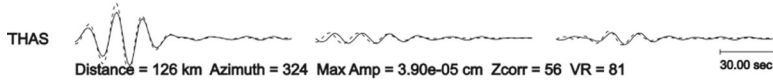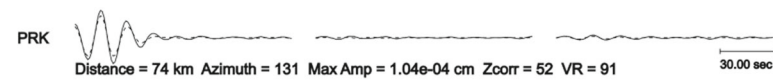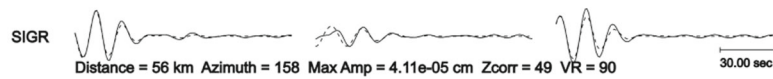Variance = 7.91e-10
Var. Red. = 91.1
RES/Pdc = 8.41e-12

7

Tangential   **Radial**   **Vertical**

LIA
Distance = 40 km Azimuth = 305 Max Amp = 1.01e-04 cm Zcorr = 38 VR = 88   20.00 sec

SIGR
Distance = 56 km Azimuth = 156 Max Amp = 3.58e-05 cm Zcorr = 40 VR = 73   20.00 sec

PRK
Distance = 76 km Azimuth = 129 Max Amp = 1.34e-04 cm Zcorr = 43 VR = 80   20.00 sec

SKY
Distance = 124 km Azimuth = 226 Max Amp = 6.11e-05 cm Zcorr = 48 VR = 82   20.00 sec

THAS
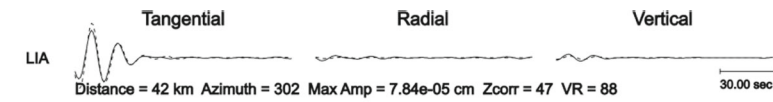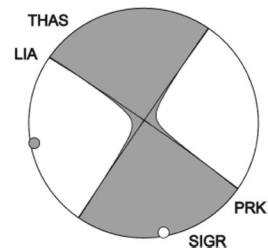Distance = 126 km Azimuth = 325 Max Amp = 4.50e-05 cm Zcorr = 47 VR = 82   20.00 sec

Depth = 8
Strike = 30 ; 299
Rake = -171 ; -3
Dip = 87 ; 81
Mo = 4.80e+21
Mw = 3.72
Percent DC = 92
Percent CLVD = 8
Percent ISO = 0
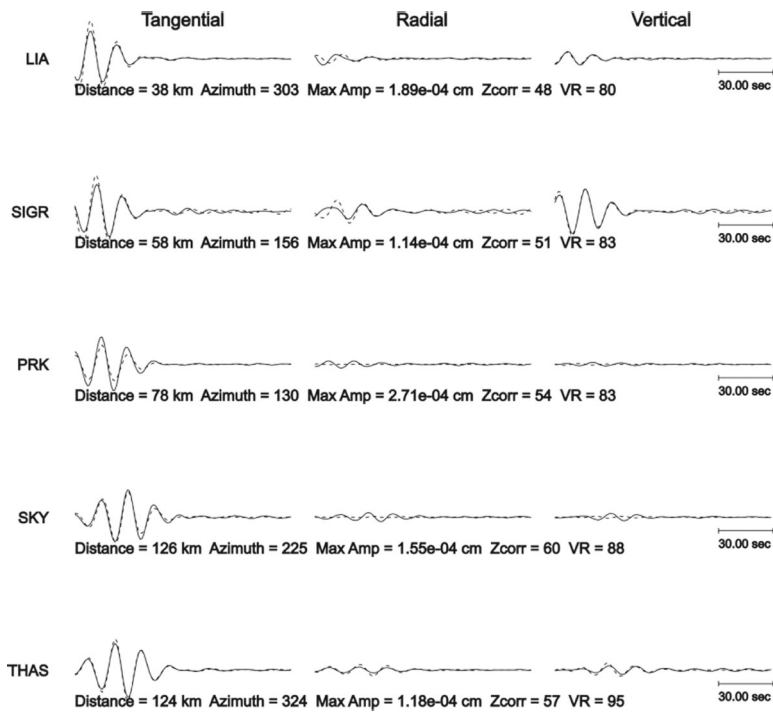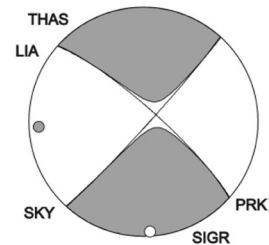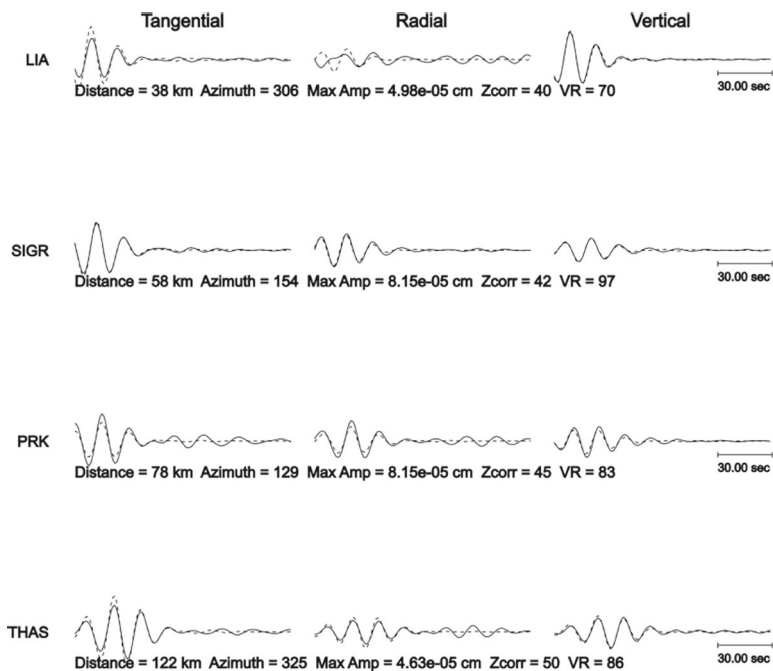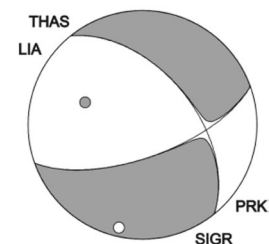Variance = 7.60e-11
Var. Red. = 81.3
RES/Pdc = 8.26e-13

8

9

10

13

14

and the corresponding beach ball. Numbering of the solutions is as in Table 1.

References

Altinok Y, Alpar B, Yaltirak C, Pinar A, zer N (2012) The earthquakes and related tsunamis of October 6, 1944 and March 7, 1867; NE Aegean Sea. Nat Hazards 60(1):3–25. doi:10.1007/s11069-011-9949-7

Benetatos C, Roumelioti Z, Kiratzi A, Melis N (2002) Source parameters of the M 6.5 Skyros Island (North Aegean Sea) earthquake of July 26, 2001. Ann Geophys 45(3–4):513–526

Brooks M, Ferentinos G (1980) Structure and evolution of the Sporades basin of the north Aegean trough, northern Aegean Sea. Tectonophysics 68(1–2):15–30. doi:10.1016/0040-1951(80)90006-2

Caputo R, Chatzipetros A, Pavlides S et al (2012) The Greek database of Seismogenic sources (GreDaSS): state-of-the-art for northern Greece. Ann Geophys 55(5):859–894. doi:10.4401/ag-5168

Chatzipetros A, Kiratzi A, Sboras S, Zouros N, Pavlides S (2013) Active faulting in the north-eastern Aegean Sea Islands. Tectonophysics 597–598:106–122, ISSN 0040-1951, doi:10.1016/j.tecto.2012.11.026

Dreger D (1994) Empirical Green's function study of the January 17, 1994 Northridge, California earthquake. Geophys Res Lett 21:2633–2636

Dreger D (2002) Time-domain moment tensor INVerse code (TDMT_INVC) Version 1.1, Berkeley Seismological Laboratory, 18

Dreger DS (2003) TDMT_INV: time domain seismic moment tensor INVersion, international handbook of earthquake and engineering seismology. In: Lee WHK, Kanamori H, Jennings PC, Kisslinger C (eds), vol. B. Academic Press, London, p 1627

Dreger D, Helmberger D (1993) Determination of source parameters at regional distances with single station or sparse network data. J Geophys Res 98:8107–8125

Ganas A, Drakatos G, Pavlides SB, Stavrakakis GN, Ziazia M, Sokos E, Karastathis VK (2005) The 2001 Mw=6.4 Skyros earthquake, conjugate strike–slip faulting and spatial variation in stress within the central Aegean Sea. J Geodyn 39:61–77

Ganas A, Roumelioti Z, Chousianitis K (2012) Static stress transfer from the May 20, 2012, M 6.1 Emilia-Romagna (northern Italy) earthquake using a co-seismic slip distribution model. Ann Geophys, Special Issue entitled "The Emilia seismic sequence of May–June, 2012: preliminary data and results". 55(4) doi:10.4401/ag-6176

Gomberg J, Reasenberg PA, Bodin P, Harris RA (2001) Earthquake triggering by seismic waves following the Landers and Hector mine earthquakes. Nature 411:462–466

Harris RA, Simpson RW (1998) Suppression of large earthquakes by stress shadows: a comparison of Coulomb and rate and state failure. J Geophys Res 103:439–451

Hartzell SH (1978) Earthquake aftershocks as Green's functions. Geophys Res Lett 5(1):1–4

Hatzfeld D, Ziazia M, Kementzetzidou D, Hatzidimitriou P, Panagiotopoulos D, Makropoulos K, Papadimitriou P, Deschamps A (1999) Microseismicity and focal mechanisms at the western termination of the North Anatolian Fault and their implications for continental tectonics. Geophys J Int 137:891–908

Kalogeras, I., Melis, N., Evangelides, C., (2013) The earthquake of January 8, 2013 at SE of Limnos Island, Northern Aegean, Greece. NOA online report at http://www.gein.noa.gr/Documents/pdf/Report_EN_PDF.pdf (last accessed 23 December 2013)

Karabulut H, Roumelioti Z, Benetatos C, Mutlu A, Ozalaybey S, Aktar M, Kiratzi A (2006) A source study of the 6 July 2003 (Mw 5.7) earthquake sequence in the Gulf of Saros (Northern Aegean Sea): seismological evidence for the western continuation of the Ganos fault. Tectonophysics 412:195–216

Karagianni EE, Papazachos CB, Panagiotopoulos DG, Suhaldoc P, Vuan A, Panza GF (2005) Shear velocity structure in the Aegean area obtained by inversion of Rayleigh waves. Geophys J Int 160:127–143

Kiratzi AA, Svigkas N (2013) A study of the 8 January 2013 Mw5.8 earthquake sequence (Lemnos Island, East Aegean Sea). Tectonophysics 608:452–460

Kiratzi AA, Wagner GS, Langston CA (1991) Source parameters of some large earthquakes in northern Aegean determined by body waveform inversion. Pure Appl Geophys 135(4):515–527. doi:10.1007/bf01772403

Konstantinou KI, Melis NS, Boukouras K (2010) Routine regional moment tensor inversion for earthquakes in the Greek region; the National Observatory of Athens (NOA) database (2001–2006). Seismol Res Lett 81(5):750–760

Koukouvelas IK, Aydin A (2002) Fault structure and related basins of the North Aegean Sea and its surroundings. Tectonics 21(5), doi:10.1029/2001TC901037

Kreemer C, Chamot-Rooke N, Le Pichon X (2004) Constraints on the evolution and vertical coherency of deformation in the Northern Aegean from a comparison of geodetic, geologic and seismologic data. Earth Planet Sci Lett 225(3–4):329–346. doi:10.1016/j.epsl.2004.06.018

Le Meur H (1994) Tomographie tridimensionnelle a partir des temps des premieres arrivees des ondes P et S, application a la region de Patras (Grece). PhD thesis, Paris VII, France (in French)

Le Meur H, Virieux J, Podvin P (1997) Seismic tomography of the gulf of Corinth: a comparison of methods. Ann Geofis 40(6):1–24

Lin J, Stein R (2004) Stress triggering in thrust and subduction earthquakes, and stress interaction between the southern San Andreas and nearby thrust and strike–slip faults. J Geophys Res 109, B02303. doi:10.1029/2003JB002607

Lomax A, Virieux J, Volant P, Berge C (2000) Probabilistic earthquake location in 3D and layered models: introduction of a Metropolis–Gibbs method and comparison with linear locations. In: Thurber CH, Rabinowitz N (eds) Advances in seismic event location. Kluwer, Amsterdam, pp 101–134

Makropoulos K, Kaviris G, Kouskouna V (2012) An updated and extended earthquake catalogue for Greece and adjacent areas since 1900. Nat Hazards Earth Syst Sci 12:1425–1430

Michael AJ (1991) Spatial variations in stress within the 1987 Whittier narrows, California, aftershock sequence — new techniques and results. J Geophys Res 96(B4):6303–6319. doi:10.1029/91JB00195

Mori J, Hartzell S (1990) Source inversion of the 1988 Upland earthquake: determination of a fault plane for a small event. Bull Seismol Soc Am 80:278–295

Müller MD, Geiger A, Kahle H, Veis G, Billiris H, Paradissis D, Felekis S (2013) Velocity and deformation fields in the north Aegean domain, Greece, and implications for fault kinematics, derived from GPS data 1993–2009. Tectonophysics 597–598:34–49

Nalbant SS, Hubert A, King GCP (1998) Stress coupling between earthquakes in northwest Turkey and the north Aegean Sea. J Geophys Res 103(B10):24469–24486. doi:10.1029/98JB01491

Novotný O, Zahradník J, Tselentis G-A (2001) North-Western Turkey earthquakes and the crustal structure inferred from surface waves observed in Western Greece. Bull Seismol Soc Am 91:875–879

Okada Y (1992) Internal deformation due to shear and tensile faults in a half-space. Bull Seismol Soc Am 82:1018–1040

Panagiotopoulos DG, Hatzidimitriou PM, Karakaisis GF, Papadimitriou EE, Papazachos BC (1985) Travel time residuals in southeastern Europe. Pure Appl Geophys 123:221–231

Papadimitriou EE, Sykes LR (2001) Evolution of the stress field in the northern Aegean Sea (Greece). Geophys J Int 146(3): 747–759. doi:10.1046/j.0956-540x.2001.01486.x

Papadopoulos G, Ganas A, Plessa A (2002) The Skyros earthquake (Mw6.5) of 26 July 2001 and precursory seismicity patterns in the North Aegean Sea. Bull Seismol Soc Am 92(30):1141–1145

Pasyanos M, Dreger D, Romanowicz B (1996) Towards real-time determination of regional moment tensors. Bull Seismol Soc Am 86:1255–1269

Pavlides SB, Tranos MD (1991) Structural characteristics of 2 strong earthquakes in the north-Aegean — Ierissos (1932) and Agios-Efstratios (1968). J Struct Geol 13(2):205–214. doi:10.1016/0191-8141(91)90067-s

Podvin P, Lecomte I (1991) Finite difference computation of traveltimes in very contrasted velocity models: a massively parallel approach and its associated tools. Geophys J Int 105: 271–284

Roumelioti Z, Dreger D, Kiratzi A, Theodoulidis N (2003) Slip distribution of the September 7, 1999 Athens earthquake inferred from an empirical Green's function study. Bull Seismol Soc Am 93(2):775–782

Roumelioti Z, Benetatos C, Kiratzi A (2011) Time Domain Moment Tensors of earthquakes in the broader Aegean Sea for the years 2006–2007: the database of the Aristotle University of Thessaloniki. J Geodyn 51:179–189

Saikia CK (1994) Modified frequency–wavenumber algorithm for regional seismograms using Filon's quadrature; modeling of Lg waves in eastern North America. Geophys J Int 118:142–158

Tarantola A (1987) Inverse problem theory: methods f8or data fitting and model parameter estimation. Elsevier, Amsterdam, 613p

Tarantola A, Valette B (1982) Inverse problems = quest for information. J Geophys 50:159–170

Taymaz T, Jackson J, Mckenzie D (1991) Active tectonics of the north and central Aegean Sea. Geophys J Int 106(2):433–490. doi:10.1111/j.1365-246X.1991. tb03906.x

Toda S, Stein RS, Richards-Dinger K, Bozkurt S (2005) Forecasting the evolution of seismicity in southern California: animations built on earthquake stress transfer. J Geophys Res 110:B05S16, doi:10.1029/2004JB003415

Tselentis G, Zahradnik J (2000) The Athens earthquake of 7 September 1999. Bull Seismol Soc Am 90:1143–1160

Wiemer S (2001) A software package to analyse seismicity: ZMAP. Seismol Res Lett 72(2):374–383

Yaltirak C, Alpar B (2002) Kinematics and evolution of the northern branch of the North Anatolian Fault (Ganos Fault) between the Sea of Marmara and the Gulf of Saros. Mar Geol 190(1–2):351–366. doi:10.1016/S0025-3227(02)00354-7